Materials Horizons

Accepted Manuscript

This article can be cited before page numbers have been issued, to do this please use: K. Intonti, A. Mazzotti, A. Pelella, F. Giubileo, N. Martucciello, S. O'sullivan, V. Patil, P. Hurley, L. Ansari, F. Gity and A. Di Bartolomeo, *Mater. Horiz.*, 2026, DOI: 10.1039/D5MH01871D.

ROYAL SOCIETY OF CHEMISTRY

rsc.li/materials-horizons

New Concepts

View Article Online
DOI: 10.1039/D5MH01871D

We report a new mechanism to achieve anti-ambipolar transport in a WSe_2-based field-effect transistor (FET) through a light-tunable transition from its intrinsic ambipolar behavior. While anti-ambipolar responses in 2D devices have so far been primarily realized in carefully engineered heterostructures, our work demonstrates that illumination alone is sufficient to reconfigure the transport regime of a single-material device. In the dark, the transistor exhibits ambipolar characteristics with dominant n-type conduction, but under controlled optical excitation it evolves into a clear anti-ambipolar profile.

This light-driven transition is not only reversible and reproducible but also allows the definition of three distinct current states, enabling ternary logic operation without the need for complex heterojunction architectures. The peak current scales linearly with illumination intensity, showing that optical excitation provides a powerful handle for modulating device behavior. In this way, the same WSe_2 FET integrates logic functionality and photodetection within a compact platform, bridging computation and sensing.

By shifting the focus from structural engineering to optical control, this concept establishes a versatile route for next-generation optoelectronic systems. The ability to tune transport regimes by light offers new degrees of freedom for designing reconfigurable, low-cost, and multifunctional circuits that combine speed, energy efficiency, and scalability.

Data availability statement

View Article Online
DOI: 10.1039/D5MH01871D

The data supporting the findings of this study are available from the corresponding authors upon reasonable request.

Ambipolar to anti-ambipolar light induced transition in WSe_2-based FETs

Kimberly Intonti[1,2,*], Adolfo Mazzotti[1], Aniello Pelella[1], Filippo Giubileo[2], Nadia Martucciello[2], Stephen O'Sullivan [3], Vilas Patil[3], Paul K. Hurley[3,4], Lida Ansari[3], Farzan Gity[3], and Antonio Di Bartolomeo[1,*]

[1]*Department of Physics "E. R. Caianiello", University of Salerno, via Giovanni Paolo II, Fisciano, Salerno, 84084, Italy*

[2]*CNR-SPIN Salerno, via Giovanni Paolo II, Fisciano, 84084, Italy*

[3]*Tyndall National Institute, University College Cork, Lee Maltings, Dyke Parade, Cork, T12 R5CP, Ireland*

[4]*School of Chemistry, University College Cork, Cork, Ireland*

**Corresponding authors: kintonti@unisa.it, adibartolomeo@unisa.it*

Abstract

The growing need for efficient processing of large amounts of data in compact electronic systems is driving interest in investigating alternative device architectures. 2D material-based devices exhibiting anti-ambipolar behaviour represent a promising option to address this request. In this work, we investigate a WSe_2-based field-effect transistor that shows ambipolar conduction with dominant n-type behaviour in the dark. Under illumination, using either diffuse white LED light or a collimated red laser, the device exhibits a transition to anti-ambipolar transport, with a prominent current peak in a narrow driving voltage range, which is desirable for fast switching logic applications. This response allows for the identification, under controlled illumination conditions, of three distinct current levels in three different bias regions, which are suitable for implementing a three-state logic device. The peak amplitude varies linearly with light intensity, and the corresponding photodetection performance results in a significant responsivity of 0.13 A/W under red laser illumination. The light-induced transition from ambipolar to anti-ambipolar behaviour is qualitatively described through energy band diagrams, with the photocurrent peak corresponding to the n–p transition point observed in the dark.

Keyword

WSe_2, Ambipolarism, Anti-ambipolarism, three-state logic, light-driven transition

View Article Online
DOI: 10.1039/D5MH01871D

Introduction

In the latest decades, two-dimensional (2D) layered materials, particularly transition metal dichalcogenides (TMDs), have attracted widespread interest because their unique and tuneable electrical and optical characteristics make them appealing for next-generation optoelectronic and circuit applications [1–6]. In the latest years, exploiting the absence of dangling bonds and the requirement for lattice matching, van der Waals (vdW) heterostructures have been fabricated by stacking different 2D layers of these materials with several methods. Developing beyond single material-devices, these heterostructures have demonstrated significant potential in various technologies, including photodetection, transistor operation, sensing, logic devices and neural network applications[7–11].

Building on these developments, 2D materials are now being considered for next-generation logic architectures in response to the growing demands of high-speed, compact, and flexible electronics driven by advances in artificial intelligence and neuromorphic computing. To meet these challenges, novel electronic and optoelectronic logic devices, such as ternary inverters, bipolar components[12], and multi-level systems, are increasingly needed.

Recently, as a novel feature, anti-ambipolar behaviour, which contrasts with the more common ambipolar response, was found in several 2D/2D heterostructures. Anti-ambipolar behaviour refers to the drain current reaching a local maximum at a specific gate voltage, which results in an "Λ-shaped" current vs. gate voltage curve rather than the typical "V-shape" of ambipolar devices. Devices based on this feature can implement numerous logic functions, such as having more than two logic states for information storage and information transmission, which are crucial to simplify the circuit design and increase their energy efficiency.

This phenomenon was first observed in carbon nanotubes/MoS_2 p-n heterojunctions[13] by Jariwala et al. and it was attributed to the tunability with gate bias of the resistance of the p and n semiconductors in series, which affects the net series resistance of the channel.

More recently, anti-ambipolarity was investigated in 2D/2D p-n heterojunctions. The performance of these junctions depends largely on the threshold voltages of their respective p-type and n-type materials. The threshold voltage of the p material needs to be higher than the threshold voltage of the n material to have this feature, as highlighted by Li et al[14]. They fabricated p-n heterojunctions by using p-WSe_2, n-MoS_2 and n-SnS_2. Apart from choosing the right material combination, several improvement strategies, such as intentional doping and increasing carrier concentration by using thicker TMDs were discussed.

Accordingly, Sun et al.[15] combined a few-layer p-$MoTe_2$ with multi-layer n-InSe to obtain a type II band alignment, which results in an "Λ" shape of the transfer curve with a peak-to-valley ratio of 10^3. The quantum confinement effect and the strong interlayer coupling allow for modulating the bandgap and carrier concentration of 2D materials by changing their thickness. Therefore, the threshold voltage of the two components can be controlled separately by tuning the number of layers.

Lv et al.[16] found the anti-ambipolar behaviour at room temperature in both dark and illuminated conditions in a p-WSe_2/n-SnS_2 type II heterojunction. They analysed the phenomenon with an equivalent circuit model and simulations based on Poisson and drift-diffusion equations. Having a type-II heterojunction with doped n and p materials is not necessarily enough to observe anti-ambipolarism. It is needed to have a large vdW barrier at the interface, together with recombination of electrons and holes at the space charge region to have a strong peak-to-valley ratio.

Also, other combinations, such as p-$MoTe_2$/n-MoS_2[17], and BP/MoS_2[18] have been discovered to show this feature in different conditions. However, it is still a challenge to fabricate anti-ambipolar devices with reliable and consistent performance, primarily because it requires a highly accurate control on the on-set voltage and the carrier density of both n-type and p-type components. Moreover, 2D/2D heterostructures strongly

View Article Online
DOI: 10.1039/D5MH01871D

depend on precise interface quality and multi-layer fabrication processes that lead to high production costs and complexity, limiting practical deployment.

In the search for architecture based on a single material, WSe_2-based FETs have attracted significant attention. WSe_2 is a group-VI transition metal dichalcogenide (TMD) that exhibits an indirect bandgap of 1.25 eV in its bulk form, which transitions to a direct bandgap of 1.64 eV in the monolayer limit. Unlike many other semiconductors, WSe_2 typically shows p-type or ambipolar transport behavior, making it particularly attractive for a variety of electronic and optoelectronic applications.[19]

Thakar and Lodha[20] demonstrated that ambipolar and anti-ambipolar transport in a WSe_2-based field-effect transistor can be reconfigured and tuned by using a dual electrostatic control scheme. Their device employs three back gates: one controls the channel region, while the other two, connected together, modulate the regions beneath the metal contacts, affecting the Schottky barriers. By adjusting the voltages applied to these two sets of gates, the polarity of each region can be independently controlled, enabling different transport regimes depending on the chosen bias configuration. This enables the realization of multi-bit encoding schemes. The physical mechanism is similar to that in p-n junction devices.

Simpler architectures were used by Wang et al.[21], who fabricated a WSe_2-based field effect transistor with large Schottky barriers at the metal contact interfaces. Because of large barriers, in dark conditions the transistor is in the off-state, but anti-ambipolar transport occurs under light illumination. Three logic states can be identified in the transfer curve under illumination by sweeping the gate bias.

In this study, we propose a back-gate WSe_2-based field effect transistor with Ni/Au metal contacts. In dark conditions, the device shows a slight ambipolar behaviour with a dominant n-type conduction, which, under illumination, transforms into anti-ambipolar transport. The amplitude and position of the peak in the drain current are modulable by increasing the light intensity and the sweep delay in the measurement acquisition system. The phenomenon was investigated both under the illumination of a white LED ring and a monochromatic red laser. The light-induced transition from ambipolar to anti-ambipolar behaviour in WSe_2 provides multiple degrees of freedom, enabling precise tuning and control of different electronic states via gate voltage and/or illumination.

Experimental Materials

WSe_2 flakes, whose atomic structure along three axes are displayed in Figure 1a, were mechanically exfoliated by using scotch tape and successively transferred on a Si/SiO_2 (85 nm) substrate. Ni/Au (20 nm : 200 nm) metal contacts were deposited by metal evaporation and patterned through standard photolithography and lift-off processes, giving the device shown in the optical image in Figure 1b. Raman spectra acquired from other devices fabricated using the same process, confirming the structural integrity and material quality of WSe_2, are shown in Figure S.1. The asymmetry in the contacts, arising from the different geometry, is considered potentially beneficial, as similar configurations have shown useful effects in WSe_2 devices[22]. The height profiles, acquired through Atomic Force Microscopy (AFM) in contact mode, reveal that the multi-layer flake is around 50 nm thick. A representative profile is shown in Figure 1c. As mentioned above, thicker flakes enable higher carrier concentration than in thin flakes. The schematic of the device together with the measurement set up is displayed in Figure 1d. We performed electrical measurements in a two-probe configuration in a Janis probe station equipped with nanoprobes connected to the source/drain leads. The back gate voltage was applied through the sample holder of the probe station that is in direct electrical contact with the substrate. The measurements were acquired through a Keithley 4200 SCS Parameter Analyzer at room temperature and pressure. The photoresponse of the device was investigated by using a white led ring with a maximum power of 1.4 W and a Thorlabs (639 nm) red laser with a nominal power of 4.37 mW.

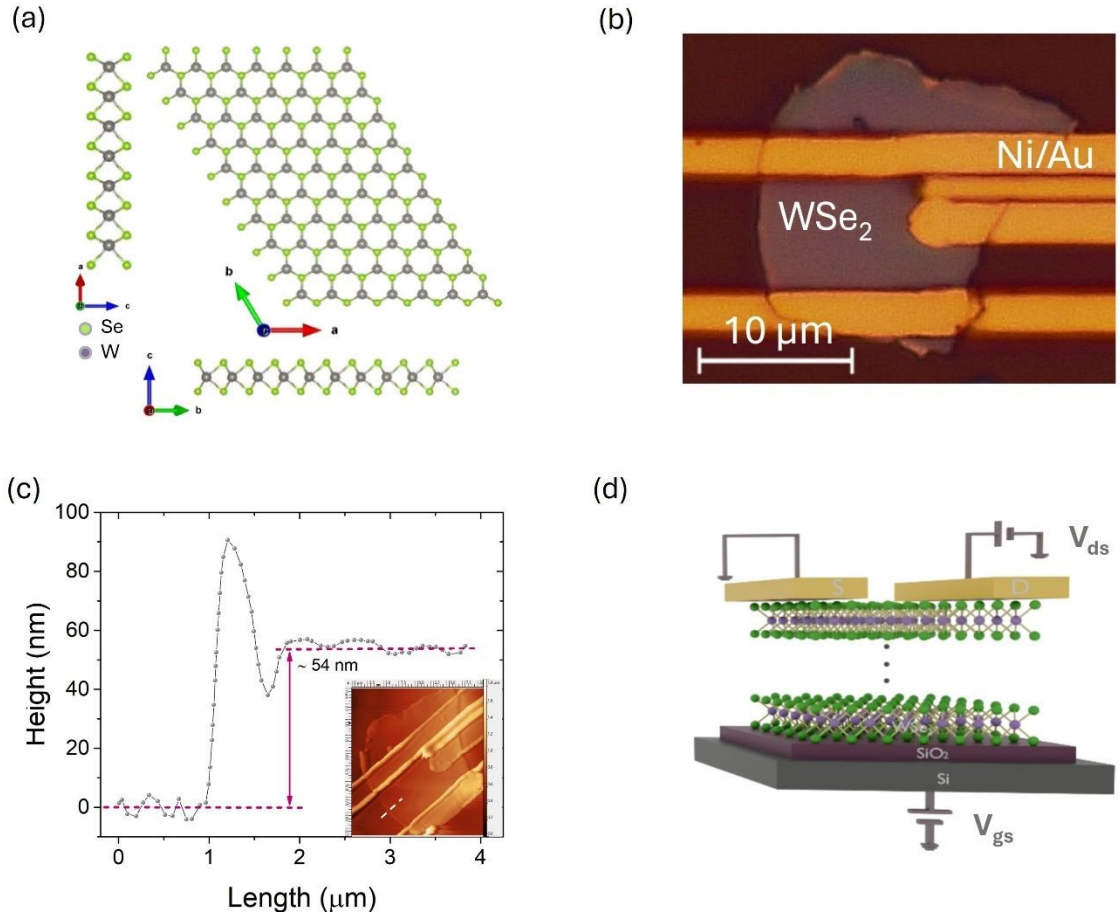

Figure 1: (a) Atomic structure of WSe2 along three axes. (b) Optical image of the WSe2-based field effect transistor with Ni/Au metal contacts. (c) AFM profile extracted from the white line represented in the AFM image in the inset. (d) Schematic of the device showing the measurement set up.

View Article Online
DOI: 10.1039/D5MH01871D

Results and Discussion

Section 1: Electrical characterization in dark conditions

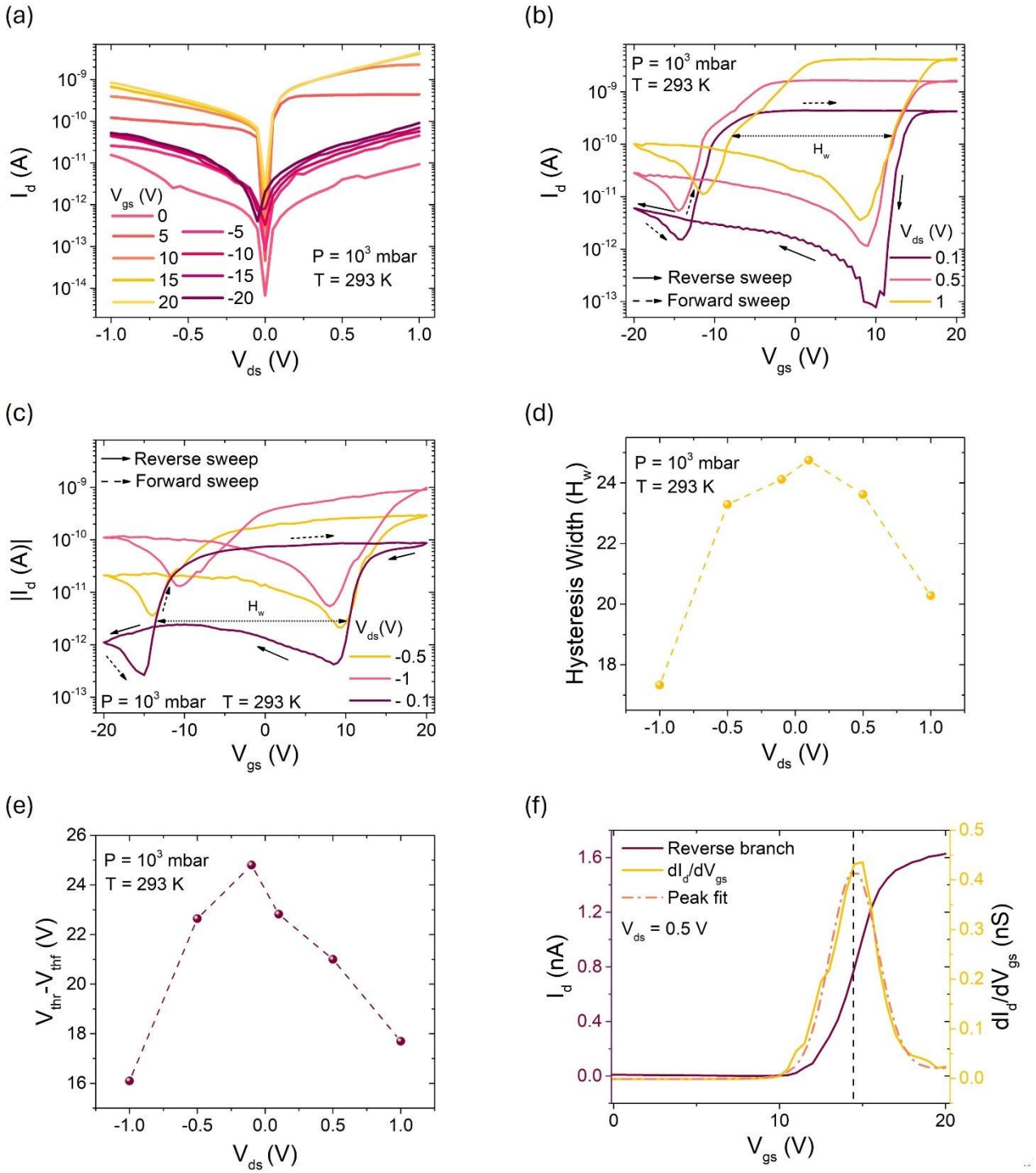

Figure 2: (a) Output curves obtained by sweeping V_{ds} between -1 and 1 V at different gate voltages. (b) Transfer curves obtained by double sweeping V_{gs} between 20 and -20 V at several positive V_{ds} and (c) negative V_{ds}. (d) Extraction of the hysteresis width from the transfer curves reported in (b) and (c). (e) Extraction of the shift in the threshold voltage between the forward and the reverse branches of the transfer curves. (f) Identification of the maximum transconductance along the reverse branch of the transfer curve at V_{ds} = 0.5 V.

View Article Online
DOI: 10.1039/D5MH01871D

We first performed electrical measurements in the dark. Figure 2a shows the output curves (I_{ds} vs V_{ds} as a function of V_{gs}) on a semi-log scale obtained by sweeping V_{ds} between -1 and 1 V and stepping V_{gs} from -20 to 20 V. At V_{gs} = 0 V, the deviation from linearity in the I_d -V_{ds} curve indicates the presence of Schottky barriers at the metal/WSe_2 interfaces [23]. The drain current is in the range of tens of pA, confirming that the contacts are highly resistive and that significant carrier injection requires applying a gate bias. We limited to ±20 V the bias applied at the gate terminal to avoid stressing the gate oxide and because the current had already reached saturation within this range. Beyond the non-linear behaviour, the output curves are also asymmetric, revealing that the two metal/semiconductor interfaces contribute differently to charge injection. In particular positive drain biases favor charge injection more effectively, consistent with asymmetric Schottky barriers at the source and drain [24,25]. This asymmetry is more pronounced at positive gate voltages. For clarity, band diagrams describing the evolution of the Schottky barriers under different gate conditions are included in Figure S.2. The drain current increases while stepping the gate bias both positively and negatively, revealing that the device shows a slight ambipolar behaviour.

The ambipolar conduction is confirmed by the transfer curves (I_d vs V_{gs} at fixed V_{ds}) in Figure 2b and 2c, acquired at positive and negative V_{ds} respectively, by sweeping V_{gs} from 20 to -20 V. Ambipolarity is related to band shift under application of an external field, which is equivalent to displace the Fermi level between the valence and the conduction band, which is possible because of the weak Fermi level pinning at the metal/WSe_2 interface. The effective polarity depends on the thickness of WSe_2 and the work function of the metal contacts [26,27]. Ni contacts enable a transition from p-type transport for thin devices to ambipolar and then n-type behaviour as WSe_2 thickness increases[28]. The dominant n-type behaviour in our device confirms that Ni Fermi level is closer to the conduction band of the 50 nm thick WSe_2, and injects electrons more easily than hole[29]. The p-type behaviour, also induced by electronegative adsorbates on the surface of the material[30,31], becomes more pronounced at higher V_{ds} since the barrier at the valence band becomes thinner.

The on-current I_{on} grows with V_{ds} both at the n and p-type side, but this does not determine an increase in the I_{on}/I_{off} ratio of the device. For the n-side it is about three orders of magnitude (10^3) at positive V_{ds} and two orders of magnitude at negative V_{ds}.

By double sweeping the gate bias, a wide hysteresis occurs, especially at the n-side. Because of the slight ambipolarity the device shows, it determines a butterfly shape in the transfer curve. The transition biases between n and p conduction, corresponding to the minimum I_d values in the transfer curves, exhibit a left shift along the reverse branch and a right shift along the forward branch, as V_{ds} increases in absolute value.

Hysteresis is predominantly due to the defective interface with the SiO_2 layer, but also to trapping mechanisms inside the material and surface-adsorbate-induced traps[32]. Measurements performed in high vacuum, indeed, reveal a narrower hysteresis.[33] Under an increasing positive gate voltage (forward sweep), the acceptor traps capture electrons, so that they can act as an additional negative gate bias during the application of a decreasing V_{gs} (reverse sweep). This produces a right shift of the threshold voltage on the reverse branch [34]. The hysteresis width, extracted as the maximum voltage distance between the reverse and forward branches, and reported in Figure 2d, increases from ~17 to 24 as V_{ds} goes from -1 to -0.1 V and lowers from ~25 to 20 V as V_{ds} increases from 0.1 to 1 V. The threshold voltage can be determined by finding the intersection between the x-axis and the linear fit of the initial (lower) portion of the transfer curve, at the onset of conduction. The separation between the threshold voltage on the reverse branch V_{thr} and on the forward branch $V_{thf,}$, consistently decreases as $|V_{ds}|$ increases, ranging from 22 to 16 V at positive V_{ds} and from 24 to 16 V at negative ones- see Figure 2e.

The maximum mobility has been calculated according to the formula:

View Article Online
DOI: 10.1039/D5MH01871D

$$\mu = g_m \frac{L}{C_{ox} W V_{ds}}$$

where g_m is the maximum transconductance, L and W are the length and width of the channel and C_{ox} = 4.06 x 10^{-8} F/cm^2 is the oxide capacitance per unit area. The electron mobility is higher than the hole one, and reaches its maximum at positive V_{ds} in correspondence with the inflexion point of the reverse branch, as pointed out by Figure 2f for the V_{ds} = 0.5 V case. However, the mobility is quite low, the maximum being around (9 ± 2)·10^{-3} cm^2/Vs. It is likely limited by scattering events with the defects of the material[35], surface states and mainly at the interface with the oxide[36], as suggested by the hysteresis. The slight variations in FET electrical parameters for positive and negative V_{ds}, including on-current, on/off ratio, mobility, and hysteresis width, support the presence of asymmetric Schottky barriers, likely due to unequal metal contact areas that cause different contact resistances at the metal interfaces[25].

Section 2: Electrical characterization under LED light

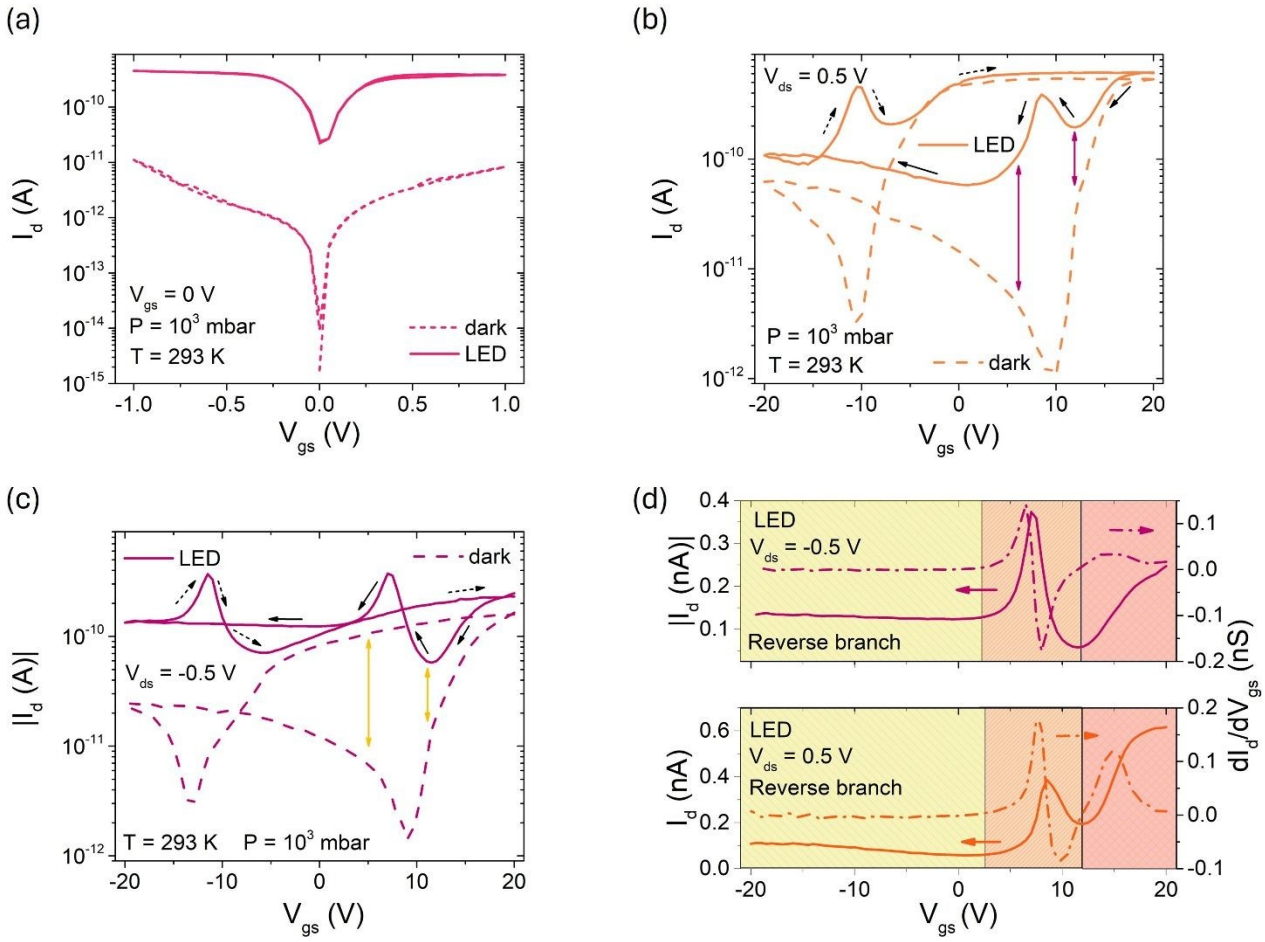

Figure 3: Comparison between (a) I_d–V_{ds} curves, (b) transfer curves at V_{ds} = 0.5 V, and (c) transfer curves at V_{ds} = −0.5 V, measured in the dark and under LED illumination. Colored arrows highlight the alignment between the inflection points of the dark transfer curves and the onset of the peak photoresponse**.** (d) The three colored regions identify distinct operating regimes along the reverse sweep (solid lines) of the transfer curves at V_{ds} = -0.5 V (top) and V_{ds} = 0.5 V (bottom). Dashed lines represent the transconductance as a function of gate voltage in each case.

The photoresponse of the device was first recorded under the illumination of a white LED ring (400-700 nm), providing broadband illumination across the visible light range, where WSe_2 exhibits high optical absorption

View Article Online
DOI: 10.1039/D5MH01871D

[37]. This allows a comprehensive evaluation of the device's behaviour under visible-light excitation, without biasing the measurement toward a specific wavelength. The I-V curve at V_{gs} = 0 V in Figure 3a shows a significant enhancement of the drain current when the light is on at both positive and negative V_{ds}. To investigate the impact of the gate bias on the drain current we measured transfer curves under light by double sweeping V_{gs} from 20 to -20 V. To emphasize the differences between the transfer characteristics in dark and illuminated conditions, a direct comparison is presented. For the sake of clarity, the analysis is restricted to V_{ds} = 0.5 V and -0.5 V - see Figure 3b and 3c, respectively, but analogous behaviour is observed at different V_{ds}.

Under illumination, the device exhibits positive photoconductivity across all gate voltages, resulting in an overall upward shift of the transfer curve compared to the dark condition. However, ambipolar transport develops into a more complex scenario, as the gate voltage modulates the channel current to produce distinct peaks at specific gate biases, indicating the onset of anti-ambipolar behavior at both positive and negative V_{ds}.

The transfer curves under illumination also exhibit hysteresis. Two separate current peaks appear during the gate voltage double sweep at fixed V_{ds}: one along the reverse sweep at positive gate voltages, and the other along the forward sweep at negative gate voltages.

In Figure 3d, the reverse branches (solid lines) of the transfer curves at V_{ds} = -0.5 V and 0.5 V are separately shown and three distinct operating regions can be identified as a function of the gate bias. (The same for the forward sweep is reported in Figure S.3). Moving from left to right, the current initially remains nearly constant for V_{gs} < 2 V (yellow region), with a gentle decreasing slope as V_{gs} increases, resembling the p-type branch of the transfer curve in the dark. The peaked regions, instead, extend between ~2 and 12.5 V (orange region). At positive V_{ds}, the current of the peak follows the shape of the transfer curve: the current level on the right side of the peak is higher than on the left, and the peak maximum does not correspond to the highest current value in the transfer curve. Conversely, the peak observed at negative V_{ds} shows the opposite trend, with the current on its right side lower than on the left, and it is more pronounced than in the positive counterpart. For V_{gs} > 12 V (pink region), the current enters a monotonically increasing region, resembling the n-branches of the dark transfer curves, and approaches saturation at positive V_{ds}.

Anti-ambipolar transport naturally gives rise to negative differential resistance (NDR), a nonlinear carrier transport phenomenon in which increasing the bias voltage leads to a reduction in current. Various architectures have been exploited to obtain it in TMD-based structures. For instance, Wang et al.[38] identified semiconducting TMDs hosting S-type NDR in a vertical electrode/TMD/electrode structure, and they attributed it to the thermal feedback conduction mechanism induced by Joule self-heating effect. Huo et al.[39], instead, proposed a VdW heterostructure made of semi-metallic Td-WTe_2 and MoS_2/$MoTe_2$, exploiting the formation of a type-III band alignment. In both cases, NDR appears as a peak in the I-V characteristics. In our case, anti-ambipolar transport manifests as negative transconductance (NTC) with respect to the gate voltage, see the dashed lines in Figure 3d. Such a feature is valuable for various emerging analog and digital applications. In the analog domain, it has been shown that single material-based transistors exhibiting the coexistence of positive and negative transconductance regions can generate in-phase, out-of-phase, and frequency-doubled signals when an AC input on the gate terminal is combined with a proper DC bias [37]. Additionally, in some anti-ambipolar architectures, the interplay between gate biasing and optical modulation has been employed to produce phase-, amplitude-, and frequency-selective output waveforms, suitable for analog modulation/encoding schemes in data communications. Multi-bit analog transmission has also been demonstrated in transistor designs that allow switching between ambipolar and anti-ambipolar transport by electrostatically control drain/source barriers and channel polarity [20]. Furthermore, NTC has been exploited to realize ternary inverters and ternary static random access memory [16,40,41].

View Article Online
DOI: 10.1039/D5MH01871D

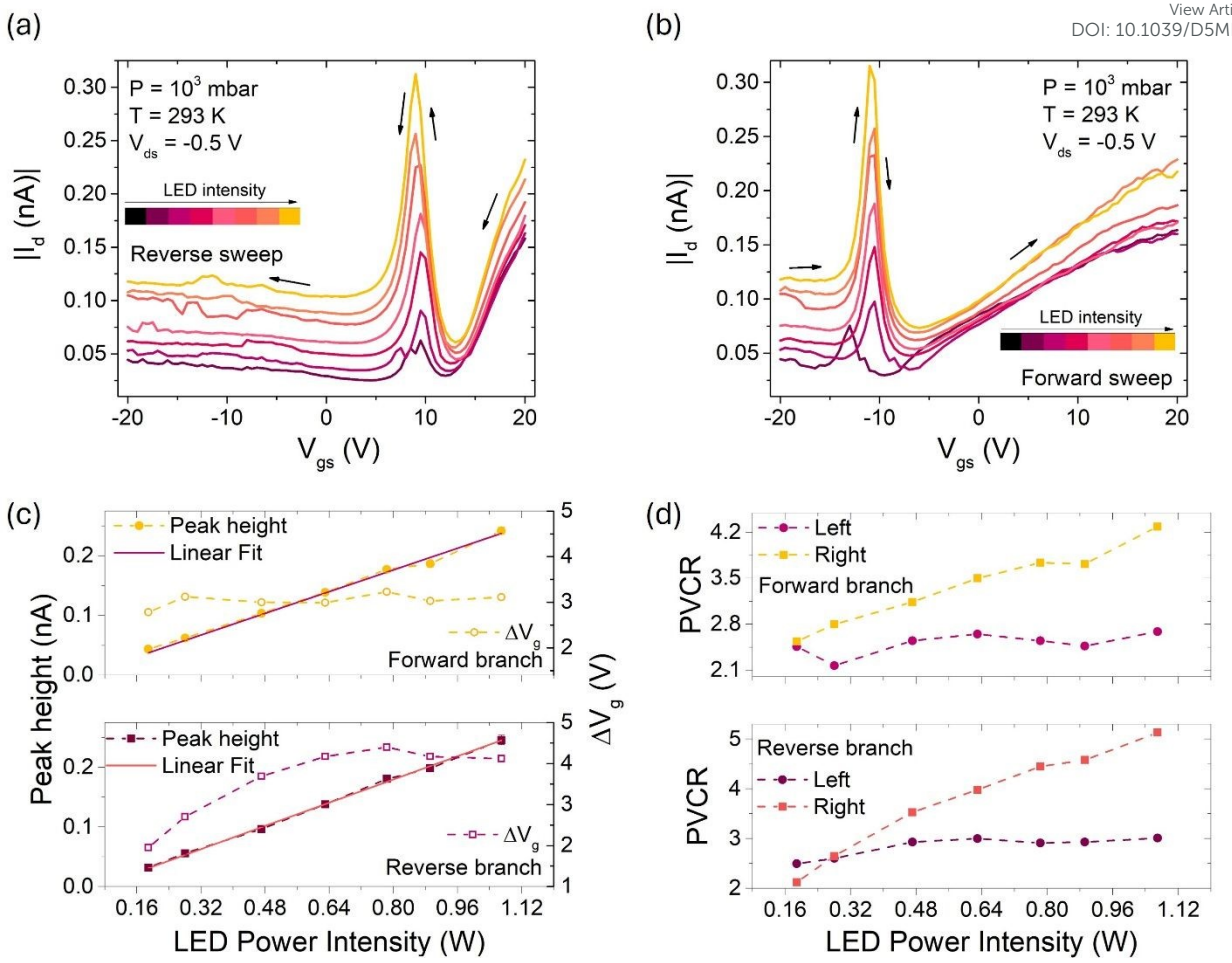

Figure 4: (a) Transfer curve under LED light obtained by reverse sweeping and (b) forward sweeping the gate bias at V_{ds} = - 0.5 V. (c) Amplitude of the peaks (left scale) and driving voltage range (right scale) extracted from the forward branch (top) and reverse branch (bottom) as a function of the LED power intensity. (d) Peak-to-valley current ratio calculated on the forward branch (top) and the reverse branch (bottom), considering the left side (square) and the right side (circle) of the peak.

Figures 4a and 4b show the reverse and forward branches of the transfer curve at V_{ds} = -0.5, respectively, under progressively stronger illumination, from 0.18 to 1.1 W. The peaks already appear at low power and get sharper with increasing intensity. At low light intensity, a dip in the current close to the maximum peak is observed along both branches; however, as the intensity increases, only one peak remains visible. Something similar was observed in $MoTe_2$-MoS_2 heterojunction, where the dip in the transconductance was related to photodoping [42]. We refer to the peak on the reverse branch as *p1* and the one on the forward branch as *p2*.

The height of the peaks evaluated with respect to the baseline is almost the same on the two branches at fixed LED intensity. It ranges from $(3.2 \pm 0.2) \cdot 10^{-2}$ to $(2.46 \pm 0.08) \cdot 10^{-1}$ nA for p1, and from $(4.4 \pm 0.3) \cdot 10^{-2}$ to $(2.42 \pm 0.06) \cdot 10^{-1}$ nA for p2, as the LED intensity increases. This value is different from the maximum current, which is slightly higher and reaches 0.31 nA, as evident from Figures 4a and 4b. When plotting the peak height as a function of the LED power, we observe a linear relationship for both p1 and p2, as indicated by the full symbols in Figure 4c. The bias voltages at which p1 and p2 appear are indicated as V_{p1} and V_{p2} in Figure S.4. As the illumination increases, the position of p1 shifts slightly to the left, because of photo-trapping processes, while V_{p2} remains nearly unchanged.

View Article Online
DOI: 10.1039/D5MH01871D

The driving voltage range (ΔV_g), defined as the voltage difference between the on-set and off-set of the peak, is narrower in our device compared to other reported devices and heterostructures[15,43], where ΔV_g typically spans several tens of volts. In our ambipolar channel, this range corresponds to the bias region where both p- and n-type conduction branches are partially active; outside this region, one mode dominates. Inflection points in the dark curves align with the onset of the photoresponse peak, as indicated by the colored arrows in Figure 3b and 3c, reflecting the overlap of the initial, resistive portions of both branches**.** This reduced ΔV_g is favourable since it enables faster and more energy-efficient switching in logic circuits[41,44]. In our measurements, ΔV_g is almost constant around 3 V in the forward sweep, while it can be tuned from approximately 2 to 4 V in the reverse sweep – see empty symbols in Figure 4c. The full width at half maximum (FWHM) of the forward peaks, indeed, are lower than the peaks on the reverse branch.

The peak-to-valley current ratio (PVCR) is not the same as the peak from the left or from the right, because of the transfer curve shape, as highlighted in Figure 4d for both the reverse and the forward branches. At the maximum LED intensity, it reaches approximately ~4 on the forward branch and ~5 on the reverse, which is lower than in heterostructures, but comparable with other WSe_2-based devices[21]. However, it needs to be improved for efficient application.

Table S.1 compares the main figures of merit of our device with those reported in the literature.

View Article Online
DOI: 10.1039/D5MH01871D

Section 3: Electrical characterization under red laser

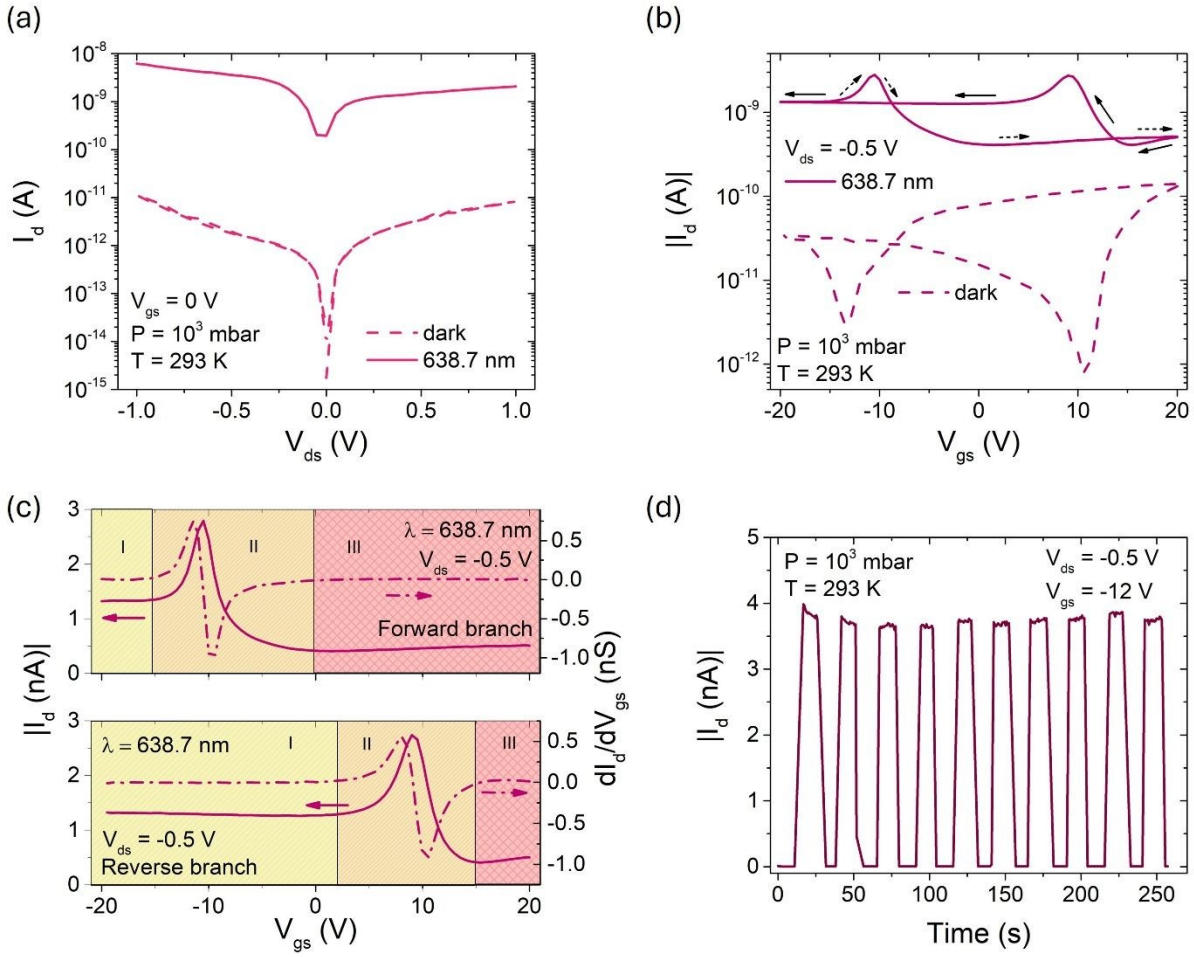

Figure 5: Comparison between (a) the I-V curves and (b) the transfer curves at Vds = -0.5 V in the dark and under red laser illumination. (c) Identification of three separate current levels (solid lines) in the forward (top) and reverse (bottom) branches of the transfer curves. Dashed lines represent the transconductance. (d) Switching behaviour of the device in response to repeated laser pulses, in correspondence of the peak on the forward branch.

To gain deeper insight into the phenomenon, the device's photoresponse was also investigated under illumination with a monochromatic red laser ($\lambda \approx 639$ nm), corresponding to a photon energy of approximately 1.94 eV. This energy lies above the WSe_2 bandgap (~1.2-1.7 eV) [45], enabling efficient photocarrier generation while avoiding high-energy induced effects. Red excitation is also standard in WSe_2 photodetector studies**.** The drain current significantly increases – see Figure 5a- by three orders of magnitude from the dark one. Figure 5b compares the transfer characteristics in dark and under light, at V_{ds} = - 0.5 V.

The overall behaviour is the same as under white light, but with a higher photocurrent. However, unlike the case under LED illumination, the forward and reverse branches of the curve can be sharply divided into three distinct current regions, as highlighted in Figure 5c at V_{ds} = -0.5 V. The same applies at positive V_{ds} – see Figure S.5. In both cases, in the yellow and pink regions, the gate bias barely modulates the drain current, which stays at two flat levels. This behaviour is due to the laser's higher local power density and spatial confinement, which generate a large concentration of carriers in a small region, locally lowering the Schottky barriers and enhancing injection. As a result, the current becomes less sensitive to gate modulation, leading to flatter response levels. Nevertheless, a prominent peak appears in the central region despite the overall saturated

View Article Online
DOI: 10.1039/D5MH01871D

regime, and the peak current is the highest obtained by sweeping the gate bias both at V_{ds} = -0.5 and 0.5 V. V_p and the driving voltage range ΔV_{gs} are consistent with that obtained under LED illumination.

In both branches in Figure 5c, the current in region I is approximately 1.33 nA, reaches a peak of 2.8 nA, and then drops to about 0.4 nA in region III. These three current levels are stable and well-defined, suggesting that the device can operate as a multi-level element under controlled illumination conditions. Multi-state devices are particularly attractive for circuit miniaturization because they can encode more information per device than binary CMOS. Whereas CMOS logic requires at least two transistors to encode a single bit, a ternary logic unit provides three distinct output states, increasing information density from 2^n to 3^n levels with the same number of units.

Considering that the peaks in the transfer curve under illumination almost coincide with the valley in the ambipolar transfer curves in dark, we investigated the dark-light switching behaviour of the device at V_{gs} = V_{p2} as this gate voltage provides the largest separation between the current values measured in dark and under illumination. The current increases quickly, reaching a steady on-state current and then decreases rapidly when the light is switched off, indicating a rapid photodetection mechanism at this bias point. From the pulses in Figure 5d, we extracted the photocurrent as [46]:

$$I_{ph} = I_{light} - I_{dark} = (3.73 \pm 0.07)\ \text{nA}$$

Defining q as the electron charge and P_{inc} = $(P/A_{spot})\cdot A_{flake}$ as the incident power, we can calculate the responsivity as

$$R = \frac{I_{ph}}{P_{inc}} \approx 0.13 \frac{A}{W},$$

and the detectivity as

$$D^* = R\sqrt{\frac{A_{flake}}{2qI_{dark}}} \approx 1.3 \times 10^{12}\ Jones$$

During operation with 10-second light pulses, the instantaneous power consumption in the ON state is ~1.85 nW, while in the dark state it drops to ~1 pW. The average power dissipation over a full light–dark cycle is below 1 nW:

$$P_{avg} = \frac{V_{ds} I_{light} t_{on} + V_{ds} I_{dark} t_{off}}{t_{on} + t_{off}} \sim 0.93\ nW$$

Additionally, the narrow driving voltage range minimizes dynamic power consumption. All these parameters highlight the anti-ambipolar transistor's promise for low-power optoelectronics.

View Article Online
DOI: 10.1039/D5MH01871D

Section 4: Mechanism

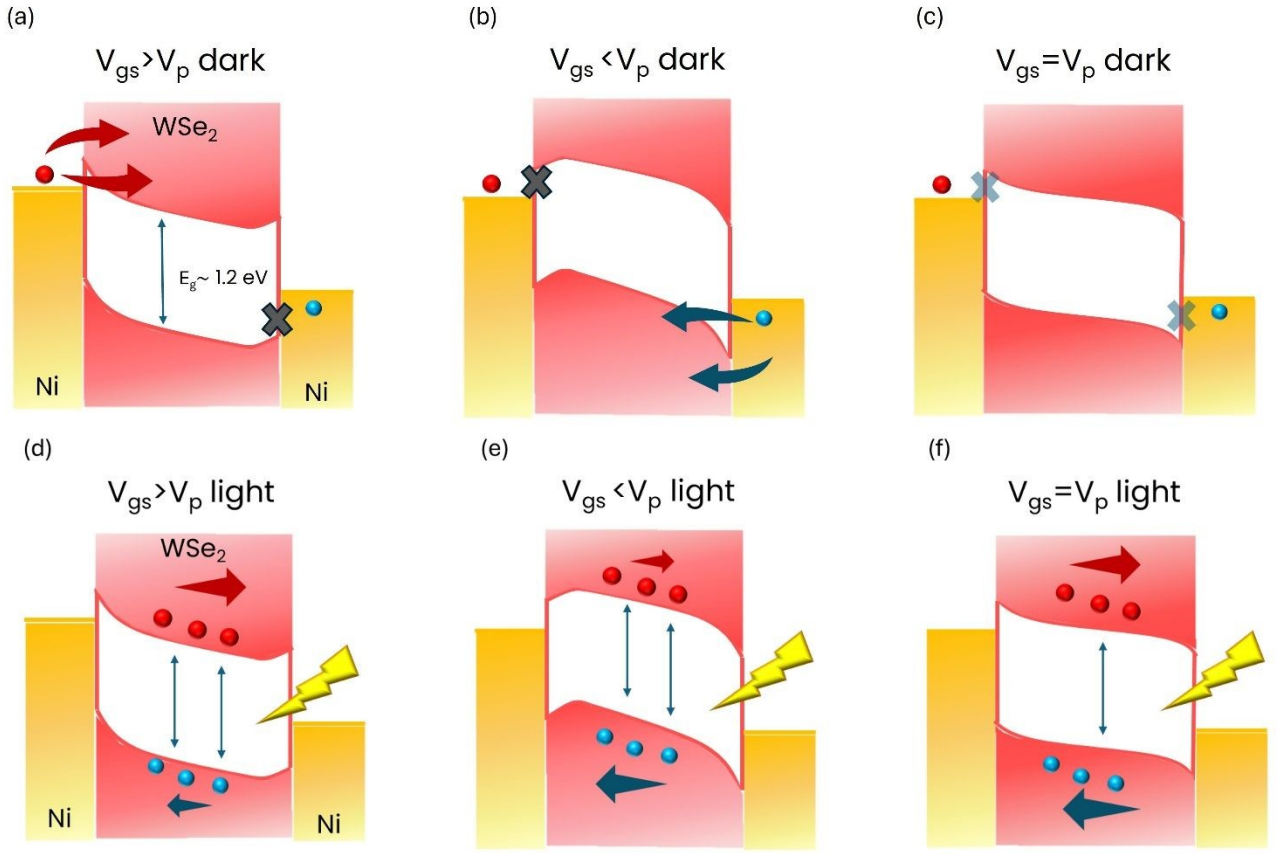

Figure 6: Band diagrams showing the band bending at the source-drain interfaces and along the channel together with the current transport in the dark at (a) $V_{gs} > V_p$, (b) $V_{gs} < V_p$; (c) $V_{gs} = V_p$. (d),(e),(f): The same under illumination.

Based on the direct comparison between the transfer curves in the dark and under illumination presented in the previous section, we observe that the on-set gate bias of ambipolarity in the dark is linked with the current peak under light. Specifically, the vertex of the V-shaped ambipolar transfer curve in the dark is related to the peak of the Λ-shaped anti-ambipolar transfer characteristic under illumination.

The correspondence between the two points is not precise because the acquisition time for the transfer curves in the dark and under illumination differs. Even with identical measurement settings, the time required to record each data point depends on the current level: lower currents, as typically observed in the dark, result in longer measurement times.

Therefore, we tried to slow down the measurement in light by adding a sweep delay (see Figure S.6) at each data point acquisition time. Under these conditions, p1 on the reverse sweep shifts to higher gate voltages, while p2 on the forward sweep shifts to lower gate voltages. This indicates that during both reverse and forward V_{gs} sweeps, reducing the sweep speed causes the peaks to appear earlier along the gate voltage axis and they better align with the minimum points of the transfer curves in the dark. This result supports our hypothesis that anti-ambipolar peaks correspond to the ambipolar transition points.

In the dark, the drain current can be described as the sum of electron and hole contributions, each enabled by thermionic emission and tunneling through a gate dependent Schottky barrier. The dominant n-type behaviour observed in Figure 2 indicates that the energy barrier for electrons injection is lower than the hole

View Article Online
DOI: 10.1039/D5MH01871D

barrier. As illustrated in Figure 6a, for $V_{gs} > V_p$, the electron barrier at the source becomes thinner, enhancing n-type conduction, while for $V_{gs} < V_p$, upward band bending at the drain side reduces the hole barrier, enabling the p-type transport (Figure 6b) [29]. At $V_{gs} = V_p$, both barriers are sufficiently large to suppress the injection of either carrier type, resulting in the minimum in the transfer curve (Figure 6c). As already mentioned, this minimum defines the transition point between n-type and p-type conduction. A small deviation from this gate voltage enables either n-type or p-type transport, depending on the direction of the sweep. This behavior is typical of Schottky-contact transistors, where carrier injection is strongly modulated by gate-controlled band bending.

Under illumination, photogenerated electron-hole pairs modify the device operation- see Figure 6d, e, and f. At gate voltages far from V_p, the device remains largely unipolar: either photo-electrons ($V_g>V_p$) or photo-holes ($V_g<V_p$) dominate the photocurrent, as the opposite carrier faces higher injection barriers and recombination processes. On the contrary, around $V_{gs} = V_p$, the band structure let both photogenerated carriers to be transferred and collected efficiently as illustrated in Figure 6f: photoelectrons can flow to the drain and holes to the source, and their simultaneous collection produces a pronounced local maximum, giving rise to the characteristic Λ shaped anti-ambipolar response. When the gate bias is at the n-p crossover, both Schottky barriers are moderately high, too high for thermal injections, but not so high to impede photogenerated carriers' transport.

Thus, the observed light-induced anti-ambipolar peak results from the combined effects of dual Schottky barrier modulation at source and drain and efficient photogeneration and separation of both carrier types across the flake at V_p because of a proper band alignment. This scenario is supported by previous reports of anti-ambipolarity in both heterojunctions and multilayer homostructures and confirms the capacity of bulk WSe_2 to host multi-state transport under optical stimulation.

Conclusion

In this work, we investigated the electrical properties of a multilayer WSe_2 based field-effect transistor, studied at room temperature and ambient pressure, both in the dark and under illumination with two different light sources. In the dark, the device exhibits ambipolar behaviour with dominant electron conduction and a characteristic butterfly-shaped transfer curve due to pronounced hysteresis. Upon illumination, the drain current increases overall but shows a peak at specific gate voltages, indicating a transition to anti-ambipolar behaviour. The amplitude of this peak can be modulated by the light intensity. The peak-to-valley ratio is such that three distinct logic states can be distinguished, particularly under illumination with a collimated red laser and a small driving voltage, making it promising for fast switching circuits. Notably, the peak in the transfer curve under illumination appears near the valley of the dark ambipolar curve, prompting a closer examination of the transient response at this point. The resulting measurements highlight promising photodetection performance and qualitative energy band diagrams are used to describe and suggest the origin of the observed transition. A systematic thickness-dependent study was not performed in this work; however, it is well established that the electrical properties of WSe_2, such as mobility, carrier type and density, screening, and Schottky barrier height, vary significantly with layer number [28,47]. Additionally, because WSe_2 exhibits relatively weak Fermi-level pinning, the balance between electron and hole injection and the position of the n–p transition point are also influenced by the alignment between the metal work function and the WSe_2 band structure[29]. Since the light-induced anti-ambipolar peak observed here is linked to this n→p crossover, variations in thickness are expected to influence whether the transition appears and at which gate voltage it occurs. These considerations suggest that a dedicated, thickness-dependent study could offer valuable insight into the tunability of the anti-ambipolar effect and may be pursued in future investigation.

View Article Online
DOI: 10.1039/D5MH01871D

Acknowledgements

A.D.B. acknowledges funding from the University of Salerno through project ORSA254881. This work was partially supported by the Research Ireland (formerly Science Foundation Ireland) AMBER Research Centre (SFI-12/RC/2278_P2). V.P. acknowledges funding from the EU-MSCA project 101153933

References

(1) Intonti, K.; Faella, E.; Kumar, A.; Viscardi, L.; Giubileo, F.; Martucciello, N.; Lam, H. T.; Anastasiou, K.; Craciun, M.; Russo, S.; Di Bartolomeo, A. Temperature-Dependent Conduction and Photoresponse in Few-Layer ReS2. *ACS Appl. Mater. Interfaces* **2023**, *15* (43), 50302–50311. https://doi.org/10.1021/acsami.3c12973.

(2) Qian, F.; Bu, X.; Wang, J.; Mao, J.-Y.; Han, S.-T.; Zhou, Y. Transistors and Logic Circuits Enabled by 2D Transition Metal Dichalcogenides: A State-of-the-Art Survey. *J. Mater. Chem. C* **2022**, *10* (45), 17002–17026. https://doi.org/10.1039/D2TC00964A.

(3) Viscardi, L.; Faella, E.; Intonti, K.; Giubileo, F.; Demontis, V.; Prete, D.; Zannier, V.; Sorba, L.; Rossella, F.; Di Bartolomeo, A. Temperature Behavior and Logic Circuit Applications of InAs Nanowire-Based Field-Effect Transistors. *Materials Science in Semiconductor Processing* **2024**, *173*, 108167. https://doi.org/10.1016/j.mssp.2024.108167.

(4) Kumar, A.; Intonti, K.; Viscardi, L.; Durante, O.; Pelella, A.; Kharsah, O.; Sleziona, S.; Giubileo, F.; Martucciello, N.; Ciambelli, P.; Schleberger, M.; Bartolomeo, A. D. Memory Effect and Coexistence of Negative and Positive Photoconductivity in Black Phosphorus Field Effect Transistor for Neuromorphic Vision Sensors. *Mater. Horiz.* **2024**, *11* (10), 2397–2405. https://doi.org/10.1039/D4MH00027G.

(5) Pelella, A.; Intonti, K.; Durante, O.; Kumar, A.; Viscardi, L.; De Stefano, S.; Romano, P.; Giubileo, F.; Neill, H.; Patil, V.; Ansari, L.; Roycroft, B.; Hurley, P. K.; Gity, F.; Di Bartolomeo, A. Multilayer WS2 for Low-Power Visible and near-Infrared Phototransistors. *Discover Nano* **2024**, *19* (1), 57. https://doi.org/10.1186/s11671-024-04000-0.

(6) Pelella, A.; Romano, P.; Intonti, K.; Viscardi, L.; Durante, O.; Capista, D.; Passacantando, M.; Giubileo, F.; Alshehri, M. A. S.; Alghamdi, M. S. G.; Craciun, M.; Russo, S.; Bartolomeo, A. D. Optoelectronic Properties of Two-Dimensional α-In2Se3 Field Effect Transistor. In *2023 IEEE Nanotechnology Materials and Devices Conference (NMDC)*; 2023; pp 270–271. https://doi.org/10.1109/NMDC57951.2023.10344214.

(7) Liang, S.-J.; Cheng, B.; Cui, X.; Miao, F. Van Der Waals Heterostructures for High-Performance Device Applications: Challenges and Opportunities. *Advanced Materials* **2020**, *32* (27), 1903800. https://doi.org/10.1002/adma.201903800.

(8) Viscardi, L.; Mazzotti, A.; Durante, O.; Pucher, T.; Martucciello, N.; Castellanos-Gomez, A.; Di Bartolomeo, A. Van Der Waals WS2/PdSe2 Heterostructure as a Visible-Light Photodetector and Pressure Optoelectronic Sensor. *2D Materials* **2025**, *12*, 045003. https://doi.org/10.1088/2053-1583/ade9da.

(9) Xu, H.; Xue, Y.; Liu, Z.; Tang, Q.; Wang, T.; Gao, X.; Qi, Y.; Chen, Y. P.; Ma, C.; Jiang, Y. Van Der Waals Heterostructures for Photoelectric, Memory, and Neural Network Applications. *Small Science* **2024**, *4* (4), 2300213. https://doi.org/10.1002/smsc.202300213.

(10) Durante, O.; De Stefano, S.; Mazzotti, A.; Viscardi, L.; Giubileo, F.; Kharsah, O.; Daniel, L.; Sleziona, S.; Schleberger, M.; Di Bartolomeo, A. Pressure-Dependent Current Transport in Vertical BP/MoS2 Heterostructures. *Heliyon* **2025**, *11* (3), e42443. https://doi.org/10.1016/j.heliyon.2025.e42443.

(11) Viscardi, L.; Durante, O.; De Stefano, S.; Intonti, K.; Kumar, A.; Pelella, A.; Giubileo, F.; Kharsah, O.; Daniel, L.; Sleziona, S.; Schleberger, M.; Di Bartolomeo, A. Dominant N-Type Conduction and Fast Photoresponse in BP/MoS2 Heterostructures. *Surfaces and Interfaces* **2024**, *49*, 104445. https://doi.org/10.1016/j.surfin.2024.104445.

(12) Han, J.; Deng, W.; Hu, F.; Han, S.; Wang, Z.; Fu, Z.; Zhou, H.; Yu, H.; Gou, J.; Wang, J. 2D Materials-Based Photodetectors with Bi-Directional Responses in Enabling Intelligent Optical Sensing. *Advanced Functional Materials n/a* (n/a), 2423360. https://doi.org/10.1002/adfm.202423360.

(13) Jariwala, D.; Sangwan, V. K.; Wu, C.-C.; Prabhumirashi, P. L.; Geier, M. L.; Marks, T. J.; Lauhon, L. J.; Hersam, M. C. Gate-Tunable Carbon Nanotube–MoS2 Heterojunction p-n Diode. *Proceedings of the National Academy of Sciences* **2013**, *110* (45), 18076–18080. https://doi.org/10.1073/pnas.1317226110.

(14) Li, Y.; Wang, Y.; Huang, L.; Wang, X.; Li, X.; Deng, H.-X.; Wei, Z.; Li, J. Anti-Ambipolar Field-Effect Transistors Based On Few-Layer 2D Transition Metal Dichalcogenides. *ACS Appl. Mater. Interfaces* **2016**, *8* (24), 15574–15581. https://doi.org/10.1021/acsami.6b02513.

(15) Sun, Y.; Gao, W.; Li, X.; Xia, C.; Chen, H.; Zhang, L.; Luo, D.; Fan, W.; Huo, N.; Li, J. Anti-Ambipolar Behavior and Photovoltaic Effect in p-MoTe2/n-InSe Heterojunctions. *J. Mater. Chem. C* **2021**, *9* (32), 10372–10380. https://doi.org/10.1039/D1TC02497C.

(16) Lv, Y.; Wu, C.-Y.; Zhao, Y.; Wu, G.; Abid, M.; Cho, J.; Choi, M.; Ó Coileáin, C.; Hung, K.-M.; Chang, C.-R.; Wu, Y.-R.; Wu, H.-C. Robust Anti-Ambipolar Behavior and Gate-Tunable Rectifying Effect in van Der Waals p–n Junctions. *ACS Appl. Electron. Mater.* **2022**, *4* (11), 5487–5497. https://doi.org/10.1021/acsaelm.2c01120.

(17) Paul, A. K.; Kuiri, M.; Saha, D.; Chakraborty, B.; Mahapatra, S.; Sood, A. K.; Das, A. Photo-Tunable Transfer Characteristics in MoTe2–MoS2 Vertical Heterostructure. *npj 2D Mater Appl* **2017**, *1* (1), 17. https://doi.org/10.1038/s41699-017-0017-3.

(18) Huang, M.; Li, S.; Zhang, Z.; Xiong, X.; Li, X.; Wu, Y. Multifunctional High-Performance van Der Waals Heterostructures. *Nature Nanotech* **2017**, *12* (12), 1148–1154. https://doi.org/10.1038/nnano.2017.208.

(19) Cheng, Q.; Pang, J.; Sun, D.; Wang, J.; Zhang, S.; Liu, F.; Chen, Y.; Yang, R.; Liang, N.; Lu, X.; Ji, Y.; Wang, J.; Zhang, C.; Sang, Y.; Liu, H.; Zhou, W. WSe2 2D P-Type Semiconductor-Based Electronic Devices for Information Technology: Design, Preparation, and Applications. *InfoMat* **2020**, *2* (4), 656–697. https://doi.org/10.1002/inf2.12093.

(20) Thakar, K.; Lodha, S. Multi-Bit Analog Transmission Enabled by Electrostatically Reconfigurable Ambipolar and Anti-Ambipolar Transport. *ACS Nano* **2021**, *15* (12), 19692–19701. https://doi.org/10.1021/acsnano.1c07032.

(21) Wang, H.; Gao, W.; Wen, P.; Yu, H.; Huang, Y.; Yue, Q.; Wang, X.; Huo, N. Light-Regulated Anti-Ambipolar Transport with Multi-Logic States in Metal-WSe2-Metal Transistor. *Advanced Electronic Materials* **2022**, *8* (12), 2200649. https://doi.org/10.1002/aelm.202200649.

(22) Zhou, C.; Zhang, S.; Lv, Z.; Ma, Z.; Yu, C.; Feng, Z.; Chan, M. Self-Driven WSe2 Photodetectors Enabled with Asymmetrical van Der Waals Contact Interfaces. *npj 2D Mater Appl* **2020**, *4* (1), 1–9. https://doi.org/10.1038/s41699-020-00179-9.

(23) Grillo, A.; Di Bartolomeo, A. A Current–Voltage Model for Double Schottky Barrier Devices. *Advanced Electronic Materials* **2021**, *7* (2), 2000979. https://doi.org/10.1002/aelm.202000979.

(24) De Stefano, S.; Spuri, A.; Barbella, R.; Durante, O.; Mazzotti, A.; Sessa, A.; Di Bernardo, A.; Di Bartolomeo, A. Multilayer MoS2 Schottky Barrier Field Effect Transistor. *IEEE Open Journal of Nanotechnology* **2025**, *6*, 51–57. https://doi.org/10.1109/OJNANO.2025.3553692.

(25) Di Bartolomeo, A.; Grillo, A.; Urban, F.; Iemmo, L.; Giubileo, F.; Luongo, G.; Amato, G.; Croin, L.; Sun, L.; Liang, S.-J.; Ang, L. K. Asymmetric Schottky Contacts in Bilayer MoS2 Field Effect Transistors. *Advanced Functional Materials* **2018**, *28* (28), 1800657. https://doi.org/10.1002/adfm.201800657.

(26) Wang, Z.; Li, Q.; Chen, Y.; Cui, B.; Li, Y.; Besenbacher, F.; Dong, M. The Ambipolar Transport Behavior of WSe2 Transistors and Its Analogue Circuits. *NPG Asia Mater* **2018**, *10* (8), 703–712. https://doi.org/10.1038/s41427-018-0062-1.

(27) Pudasaini, P. R.; Oyedele, A.; Zhang, C.; Stanford, M. G.; Cross, N.; Wong, A. T.; Hoffman, A. N.; Xiao, K.; Duscher, G.; Mandrus, D. G.; Ward, T. Z.; Rack, P. D. High-Performance Multilayer WSe2 Field-Effect Transistors with Carrier Type Control. *Nano Res.* **2018**, *11* (2), 722–730. https://doi.org/10.1007/s12274-017-1681-5.

(28) Zhou, C.; Zhao, Y.; Raju, S.; Wang, Y.; Lin, Z.; Chan, M.; Chai, Y. Carrier Type Control of WSe2 Field-Effect Transistors by Thickness Modulation and MoO3 Layer Doping. *Advanced Functional Materials* **2016**, *26* (23), 4223–4230. https://doi.org/10.1002/adfm.201600292.

(29) Das, S.; Appenzeller, J. WSe2 Field Effect Transistors with Enhanced Ambipolar Characteristics. *Appl. Phys. Lett.* **2013**, *103* (10), 103501. https://doi.org/10.1063/1.4820408.

(30) Faella, E.; Intonti, K.; Viscardi, L.; Giubileo, F.; Kumar, A.; Lam, H. T.; Anastasiou, K.; Craciun, M. F.; Russo, S.; Di Bartolomeo, A. Electric Transport in Few-Layer ReSe2 Transistors Modulated by Air Pressure and Light. *Nanomaterials* **2022**, *12* (11), 1886. https://doi.org/10.3390/nano12111886.

(31) Urban, F.; Martucciello, N.; Peters, L.; McEvoy, N.; Di Bartolomeo, A. Environmental Effects on the Electrical Characteristics of Back-Gated WSe2 Field-Effect Transistors. *Nanomaterials* **2018**, *8* (11), 901. https://doi.org/10.3390/nano8110901.

(32) Ahmed, W.; Yang, L.; Zahoor, U.; Wang, F. Oxidation and Defects in WS2 and WSe2: The First-Principle Analysis of Their Monolayer and Bulk Structures. *Journal of Physics and Chemistry of Solids* **2025**, *204*, 112775. https://doi.org/10.1016/j.jpcs.2025.112775.

(33) Di Bartolomeo, A.; Urban, F.; Pelella, A.; Grillo, A.; Passacantando, M.; Liu, X.; Giubileo, F. Electron Irradiation of Multilayer PdSe2 Field Effect Transistors. *Nanotechnology* **2020**, *31* (37), 375204. https://doi.org/10.1088/1361-6528/ab9472.

(34) Intonti, K.; Faella, E.; Viscardi, L.; Kumar, A.; Durante, O.; Giubileo, F.; Passacantando, M.; Lam, H. T.; Anastasiou, K.; Craciun, M. F.; Russo, S.; Di Bartolomeo, A. Hysteresis and Photoconductivity of Few-Layer ReSe2 Field Effect Transistors Enhanced by Air Pressure. *Advanced Electronic Materials n/a* (n/a), 2300066. https://doi.org/10.1002/aelm.202300066.

(35) Wu, Z.; Luo, Z.; Shen, Y.; Zhao, W.; Wang, W.; Nan, H.; Guo, X.; Sun, L.; Wang, X.; You, Y.; Ni, Z. Defects as a Factor Limiting Carrier Mobility in WSe2: A Spectroscopic Investigation. arXiv August 6, 2016. https://doi.org/10.48550/arXiv.1608.02043.

(36) Lee, S.-Y.; Kim, S.-H.; Watanabe, K.; Taniguchi, T.; Yee, K.-J. Role of Hexagonal Boron Nitride Configuration in Gate-Induced Hysteresis of WSe2 Field-Effect Transistors. *Current Applied Physics* **2024**, *65*, 41–46. https://doi.org/10.1016/j.cap.2024.06.003.

(37) Shi, Y.; Sang, D.; Li, C.; Ge, S.; Yu, C.; Wang, Q.; Xiao, D. Recent Progress of Optoelectronic Applications Based on 2D WSe2 Nanomaterials and Heterostructures: A Review. *J. Mater. Chem. C* **2025**, *13* (36), 18555–18574. https://doi.org/10.1039/D5TC01545F.

(38) Wang, M.; Wang, C.-Y.; Wu, C.; Li, Q.; Pan, C.; Wang, C.; Liang, S.-J.; Miao, F. S-Type Negative Differential Resistance in Semiconducting Transition-Metal Dichalcogenides. *Advanced Electronic Materials* **2019**, *5* (9), 1800853. https://doi.org/10.1002/aelm.201800853.

(39) Huo, S.; Qu, H.; Meng, F.; Zhang, Z.; Yang, Z.; Zhang, S.; Hu, X.; Wu, E. Negative Differential Resistance with Ultralow Peak-to-Valley Voltage Difference in Td-WTe_2 /2H-MoS_2 Heterostructure. *Nano Lett.* **2024**, *24* (38), 11937–11943. https://doi.org/10.1021/acs.nanolett.4c03263.

(40) Lee, T.; Jung, K.-S.; Seo, S.; Lee, J.; Park, J.; Kang, S.; Park, J.; Kang, J.; Ahn, H.; Kim, S.; Lee, H. W.; Lee, D.; Kim, K. S.; Kim, H.; Heo, K.; Kim, S.; Bae, S.-H.; Kang, S.; Kang, K.; Kim, J.; Park, J.-H. Junctionless Negative-Differential-Resistance Device Using 2D Van-Der-Waals Layered Materials for Ternary Parallel Computing. *Advanced Materials* **2024**, *36* (24), 2310015. https://doi.org/10.1002/adma.202310015.

(41) Kim, J. H.; Moon, B. H.; Han, G. H. Anti-Ambipolar Transport and Logic Operation in Two-Dimensional Field-Effect Transistors Using in-Series Integration of GeAs and SnS2. *Appl. Phys. Lett.* **2024**, *124* (12), 123104. https://doi.org/10.1063/5.0197983.

(42) Paul, A. K.; Kuiri, M.; Saha, D.; Chakraborty, B.; Mahapatra, S.; Sood, A. K.; Das, A. Photo-Tunable Transfer Characteristics in MoTe2–MoS2 Vertical Heterostructure. *npj 2D Mater Appl* **2017**, *1* (1), 17. https://doi.org/10.1038/s41699-017-0017-3.

(43) Chen, S.; Jin, J.; Wang, W.; Wang, S.; Du, X.; Wang, F.; Ma, L.; Wang, J.; Wang, C.; Zhang, X.; Liu, Q. Thermally Tunable Anti-Ambipolar Heterojunction Devices. *Phys. Chem. Chem. Phys.* **2024**, *26* (35), 23438–23446. https://doi.org/10.1039/D4CP02937B.

(44) Kobashi, K.; Hayakawa, R.; Chikyow, T.; Wakayama, Y. Interface Engineering for Controlling Device Properties of Organic Antiambipolar Transistors. *ACS Appl. Mater. Interfaces* **2018**, *10* (3), 2762–2767. https://doi.org/10.1021/acsami.7b14652.

(45) Gusakova, J.; Wang, X.; Shiau, L. L.; Krivosheeva, A.; Shaposhnikov, V.; Borisenko, V.; Gusakov, V.; Tay, B. K. Electronic Properties of Bulk and Monolayer TMDs: Theoretical Study Within DFT Framework (GVJ-2e Method). *physica status solidi (a)* **2017**, *214* (12), 1700218. https://doi.org/10.1002/pssa.201700218.

(46) Malik, M.; Iqbal, M. A.; Choi, J. R.; Pham, P. V. 2D Materials for Efficient Photodetection: Overview, Mechanisms, Performance and UV-IR Range Applications. *Frontiers in Chemistry* **2022**, *10*.

(47) Chen, V.; Lee, H. R.; Köroğlu, Ç.; McClellan, C. J.; Daus, A.; Pop, E. Ambipolar Thickness-Dependent Thermoelectric Measurements of WSe2. *Nano Lett.* **2023**, *23* (10), 4095–4100. https://doi.org/10.1021/acs.nanolett.2c03468.